Theory for the experimental observation of chaos in a rotating waterwheel

Miroslav Kolář
The Institute of Physical and Chemical Research (RIKEN), Wako-shi, Saitama, 351-01 Japan

Godfrey Gumbs*
Department of Physics, Massachusetts Institute of Technology, Cambridge, Massachusetts 02139
(Received March 28, 1991; revised mansucript received 24 September 1991)

We study the chaos for a set of coupled, nonlinear partial differential equations that originate from the equation of motion and the Fourier transform of the mass-conservation equation for the Malkus waterwheel. Dissipation for this system is produced by an adjustable brake. The braking force, proportional to the angular velocity of the wheel, is responsible for the appearance of chaos. The variation of the moment of inertia with time is taken into account. In the large-time limit, the moment of inertia of the composite system, consisting of the wheel and water, tends to a constant, and the three controlling equations of the set of coupled limit equations reduce to a special case of the Lorenz equations, in which the Rayleigh number ρ (here characterizing the distribution of water inflow along the perimeter of the wheel) can also assume negative values. Chaotic attractors of the higher harmonics of the water density have been investigated. Boundaries between various regimes of the wheel's limit behavior (uniform rotation, periodic reversals of spin, chaotic reversals) in the Lorenz parameter space have been found. The Lorenz parameter space has thus been explored in considerably more detail than by previous authors.

PACS number(s): 05.45.+b, 02.60.+y

I. INTRODUCTION

Over the years many papers have dealt with examples of equations whose solutions demonstrate nonperiodic behaviors. In this paper we study a classical system that comprises the equations of motion subject to mass conservation for water in a rotating cylindrical wheel. This apparatus was built by Professor Malkus of the Massachusetts Institute of Technology to demonstrate the nonpredictability of the motion of a dynamical system. The derived equations are similar in nature to those describing fluid convection subjected to a gravitational field as well as heating and/or cooling [1]. The differential equations introduced by Lorenz [2] are a specific subset of these equations in an infinite-dimensional phase space. We now describe the system under consideration.

In this problem, water pours in at the top of a right circular cylindrical wheel at a steady rate Q through jets that are symmetrically located just above a portion of its perimeter. The radius of the cylinder is r and along its circumference there are thin compartments into which the water from the jets enters. The axis of the cylinder is tilted so that its axis of rotation makes an angle with the vertical. An adjustable brake is attached to the cylinder. Each chamber has a hole in its bottom. Because of the symmetrical location of the jets, the wheel can never start when exactly at rest, initially. If most of the water inflow Q is concentrated near the lowest point of the wheel, the wheel comes back to rest rapidly regardless of the magnitude of its initial spin. If the water inflow is concentrated near the highest point of the wheel, what happens depends on the rate of this inflow. If the flow of water is slow, the top chambers never fill up enough to overcome the frictional forces and the wheel comes to rest shortly after it is given an initial spin. If the flow is faster, the top chambers gain weight and set the wheel in motion. The waterwheel can then settle into a rotation that continues at a steady rate. But if the flow is faster still, the spin can become chaotic, because of nonlinear effects on the system. As the chambers pass under the jets, how much they fill will depend on the speed of spin. If the wheel is spinning rapidly, the water compartments have little time to fill up. Also, for rapid motion, the compartments can start up the other side before they have time to empty. As a result, heavy chambers on one side can cause the spin to slow down and then reverse.

This paper is organized as follows. In Sec. II we derive the torque-balance equation as well as the equation governing the conservation for the mass density of water distributed around the wheel. Written in Fourier space, three of these equations decouple from the rest and determine the rotational spin of the wheel completely. In the limit of large time, these equations are exactly the same as the well-known Lorenz equations. The higher-order harmonics can only determine the details showing how the water compartments are filled. Our derivation of the torque-balance equation and the conservation of the mass density of water, as well as the analysis leading to the Lorenz equations, are based closely on the work of Strogatz [3]. We also compare the limit equations with their forms when friction is neglected. Section III is devoted to an analysis of the coupled equations for the higher harmonics of water density. All solutions of these harmonics are bounded in phase space. All trajectories converge towards a single trajectory — an attractor — which must lie inside or on a circle centered at the ori-

gin. The nature of the limit behavior of higher modes is fully determined by the angular velocity of the wheel. In Sec. IV we present and discuss our numerical results and compare them with those presented in the monograph by Sparrow [4]. One of the important contributions of this paper is obtaining a better understanding of the Lorenz model itself. This has been achieved by exploring its parameter space in detail. Our results are summarized in Fig. 11, which shows a previously unsuspected structure of periodic windows embedded in the chaotic region.

II. MATHEMATICAL FORMULATION OF THE PROBLEM

Let $u(t)$ be the tangential velocity of a point on the rim of the wheel so that $\omega(t) = u(t)/r$ is its angular velocity at time t. Let θ be the angle of rotation in the laboratory frame so that $\theta = 0$ refers to the highest point on the rim of the wheel (see Fig. 1). Let A be the cross-sectional area (perpendicular to the perimeter of the wheel) of the compartments and $P(\theta,t)$ the mass density of water, distributed as a function of angle around the wheel. We now derive the partial-differential equations for P and u, the first of which concerns the conservation of mass while the second is the torque-balance equation.

For a volume R fixed in space, the mass in this region at time t is

$$M(t) = \int_R P(\theta,t)\, dV. \tag{1}$$

However,

$$\frac{dM}{dt} = -\int_{\partial R} P(\theta,t)\, \mathbf{u}\cdot\hat{\mathbf{n}}\, dA + \int_R Q(\theta)\, dV - K\int_R P(\theta,t)\, dV, \tag{2}$$

where $\hat{\mathbf{n}}$ is the unit outward normal of the boundary (∂R) of R. The first term on the right-hand side of Eq. (2) is the rate of transport of water across the boundary ∂R due to the rotation of the wheel and the second term is the inflow due to water being pumped in through the jets.

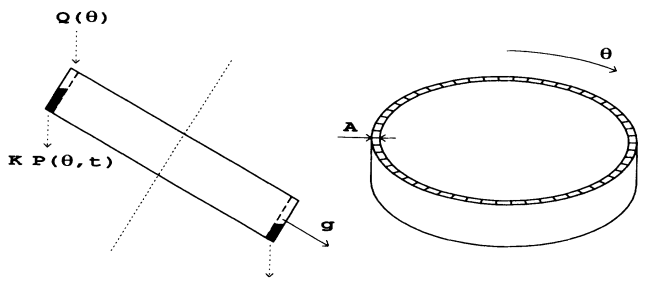

FIG. 1. Side view (section) and front view of the Malkus waterwheel. The dashed line represents the tilted axis of the wheel. The dashed arrows indicate the places where water is pumped into the waterwheel at a constant rate $Q(\theta)$ and where it leaks out through the bottom of the wheel compartments at a rate $K\ P(\theta,t)$.

The third term is due to the leakage of water through the bottom where the pressure head is proportional to the mass of water and K is a constant. Invoking the divergence theorem, we write all terms as integrals over volume. Since $\nabla\cdot(P\mathbf{u}) = \omega\,\partial P/\partial\theta$ and R is arbitrary, Eqs. (1) and (2) jointly give the mass-conservation equation

$$\frac{\partial P}{\partial t} = -\omega(t)\frac{\partial P(\theta,t)}{\partial\theta} + Q(\theta) - KP(\theta,t). \tag{3}$$

Newton's law of motion yields the torque-balance equation

$$\frac{d}{dt}[I(t)\omega(t)] = -\nu\omega(t) + Agr^2\int_0^{2\pi} P(\theta,t)\sin\theta\, d\theta, \tag{4}$$

where $I(t)$ is the total moment of inertia of the empty waterwheel (I_0) and the water added to the compartments [$I_w(t)$]. The first term on the right-hand side of Eq. (4) is the drag due to the brake where $\nu > 0$ is a constant and the second term is the gravitational torque. g is an effective gravitational constant, equal to the component of the acceleration due to gravity in the plane of the wheel perpendicular to the axis of rotation.

Assuming that $I(t) = \text{const}$ (which is true in the $t\to\infty$ limit; see below), Eqs. (3) and (4) have exactly the same form as Eqs. (1.2) and (1.1) of Ref. [1] that describe convection in fluid contained in a closed circular tube under the combined effect of the gravitational field and symmetrical heating/cooling. Heating corresponds in our waterwheel problem to water inflow and cooling to the leakage of water through the bottom of individual compartments. This is a nice example of the similarity of two rather different physical processes based on similar geometrical configurations of the two systems.

We solve Eqs. (3) and (4) by using Fourier analysis. Since $P(\theta,t)$ is 2π-periodic in θ, we write P as a Fourier series

$$P(\theta,t) = \sum_{n=0}^{\infty}[a_n(t)\sin(n\theta) + b_n(t)\cos(n\theta)]. \tag{5}$$

Also, since water is added *symmetrically*, not in a biased way, we have

$$Q(\theta) = \sum_{n=0}^{\infty} q_n\cos(n\theta), \tag{6}$$

where q_n is independent of time since the flow is constant. Making use of Eqs. (5) and (6) in Eqs. (3) and (4), a straightforward calculation yields

$$\frac{da_n}{dt} = n\omega b_n - Ka_n\ , \tag{7a}$$

$$\frac{db_n}{dt} = -n\omega a_n - Kb_n + q_n\ , \tag{7b}$$

$$\frac{d}{dt}[I(t)\omega(t)] = -\nu\omega + \pi Agr^2 a_1\ . \tag{7c}$$

Equations similar to Eqs. (7) for $n = 1$ have also been de-

rived in Appendix B of Ref. [4] when the axis of rotation of the Malkus waterwheel is horizontal. However, in this case, the derived equations correspond to a much cruder approximation of a real system [4] than the case we investigate here when the axis is inclined, where the only approximation we make is to replace the finite-sized compartments by a continuum of infinitesimally small ones. Initially, the wheel is empty, i.e., $a_n = b_n = 0$ for all n. Before we further analyze Eqs. (7), we note that the moment of inertia of the water is

$$I_w(t) = r^2 \int_R P(\theta,t)dV = r^3 A \int_0^{2\pi} P(\theta,t)d\theta. \quad (8a)$$

Substituting Eq. (5) into Eq. (8a), we obtain

$$I_w(t) = 2\pi A r^3 b_0(t). \quad (8b)$$

Setting $n=0$ in Eq. (7b), we solve the resulting nonhomogeneous differential equation for b_0 by introducing an integration factor and using the initial condition $b_0 = 0$ at $t=0$. Our calculation gives

$$I(t) = I_0 + 2\pi r^3 A \frac{q_0}{K}\left(1 - e^{-Kt}\right). \quad (9)$$

Therefore, the time dependence of the moment of inertia $I(t)$ is known in advance; it is completely decoupled from the time dependence of the velocity of the wheel. That is, we are left with Eqs. (7) in which $I(t)$ is known and given by Eq. (9).

Using this result for $I(t)$, it is clear that the equations for ωa_1, and ωb_1 [Eqs. (7a) and (7b) for $n=1$ and Eq. (7c)] decouple from all the other modes. ωb_1 and ωa_1 are quadratic nonlinear, which results in a dynamical system of three ordinary, coupled differential equations. We now introduce the following notation:

$$\rho = \frac{\pi A g r^2 q_1}{K^2 \nu}, \quad (10a)$$

$$\sigma = \frac{\nu}{K I(\infty)} = \frac{\nu}{K I_0 + 2\pi r^3 A q_0}, \quad (10b)$$

$$\Delta \equiv \frac{I(\infty) - I(0)}{I(0)} = \frac{2\pi r^3 A q_0}{K I_0}, \quad (10c)$$

and new variables x, y, z, and τ such that

$$\omega = Kx, \quad (11a)$$

$$a_1 = \frac{K\nu}{\pi A g r^2} y, \quad (11b)$$

$$b_1 = -\frac{K\nu}{\pi A g r^2} z + \frac{q_1}{K}, \quad (11c)$$

$$t = \frac{\tau}{K}. \quad (11d)$$

In terms of these variables, the set of three decoupled equations becomes

$$\frac{d}{d\tau}x = \frac{(1+\Delta)\sigma(y-x) - \Delta x e^{-\tau}}{1+\Delta(1-e^{-\tau})}, \quad (12a)$$

$$\frac{d}{d\tau}y = \rho x - y - xz, \quad (12b)$$

$$\frac{d}{d\tau}z = xy - z. \quad (12c)$$

The empty wheel corresponds to $y=0$, $z=\rho$. When the wheel is at rest, we have $x=0$. With these initial conditions, the wheel would never start since it would lie on the stable manifold of the fixed point at the origin. Thus one has to give the wheel an initial spin and we shall start with the following plausible conditions: $x(0)=x_0$, $y(0)=0$, and $z(0)=\rho$, where $x_0 \neq 0$ is arbitrary. During the initial transient period, the trajectory can be highly dependent on x_0 as the moment of inertia approaches its limit value. However, the behavior of the wheel in the limit as $\tau \to \infty$ usually depends only on the parameters ρ and σ, and is determined by the following limit equations:

$$\dot{x} = \sigma(y-x), \quad (13a)$$

$$\dot{y} = \rho x - y - xz, \quad (13b)$$

$$\dot{z} = xy - z, \quad (13c)$$

(here, and in what follows, a dot denotes differentiation with respect to the rescaled time τ). These are just the well-known *Lorenz* equations [2] with $\beta=1$ [compare Eqs. (13) with Eqs. (1.7–9) of Ref. [1] or Eqs. (7.5.8) of Ref. [5]]. The main difference is that in the case of the Malkus waterwheel, the "Rayleigh number" ρ (proportional to the amplitude q_1 of the first harmonic of the water inflow) can have *any* real value, whereas $\sigma > 0$. Note that only the zeroth and first harmonics of Q have any effect on the time dependence of the angular velocity of the wheel [cf. Eqs. (10)]. The higher modes can only determine the details of the filling of the compartments, as will be discussed in the next section, but cannot influence its speed.

Although the Lorenz equations correspond to a very simplified model for real hydrodynamical flows, it has been shown that there are other mechanical and electrical systems that are accurately described by the Lorenz model. For a discussion, see Ref. [5]. The properties of the Lorenz model and especially its chaotic behavior have been studied before [2–11]. However, most of these studies were done only for the following two one-dimensional sets of parameters: $\sigma = 10$, $\beta = 8/3$ and $\rho > 0$, and $\sigma = 16$, $\beta = 4$ and $\rho > 0$ [6]. The type of the limit behavior of the Lorenz model is related to the character of the fixed points for the given parameters. Let us briefly review the situation for the special case of Eqs. (13). The origin is always a fixed point. The Lyapunov exponents at the origin are

$$\lambda_{1,2} = -\frac{\sigma+1}{2} \pm \left[\left(\frac{\sigma-1}{2}\right)^2 + \rho\sigma\right]^{1/2}, \quad \lambda_3 = -1 . \tag{14}$$

For $\rho < -\frac{1}{\sigma}\left(\frac{\sigma-1}{2}\right)^2$, λ_1 and λ_2 are complex with negative real parts. Thus, there are inward spirals near the origin. For $\rho > -\frac{1}{\sigma}\left(\frac{\sigma-1}{2}\right)^2$, all three exponents are real and λ_2 and λ_3 are always negative. Note that $\lambda_1 < 0$ if, and only if, $\rho < 1$. For all $\rho < 1$, the origin is an attractor for all phase trajectories. This means that for $\rho < 1$, the Malkus waterwheel comes to rest regardless of the magnitude of the initial spin. This is what one would expect, as this parameter range corresponds either to $q_1 < 0$ (i.e., the inflow is concentrated near the lowest point of the wheel) or $0 < q_1 < \frac{K^2\nu}{\pi A g r^2}$ (the inflow is not large enough to overcome the braking force). For $\rho > 1$, the origin is a saddle point, and there are two other fixed points C^+, C^- [7]:

$$x = y = \pm(\rho-1)^{1/2}, \quad z = \rho - 1 . \tag{15}$$

For $\sigma \leq 2$ these two fixed points are always attractors. For $\sigma > 2$ they are attractors for $\rho < \rho_2 = \frac{\sigma(\sigma+4)}{\sigma-2}$ only. Above ρ_2 they become spiraling saddle points of index 2. At ρ_2 they lose their stability in a Hopf bifurcation [7]. Contrary to the original claim of Marsden and McCracken [7], this bifurcation seems to be subcritical for all values of σ and β: it consists in the absorption by $C^{\pm}$ of unstable periodic orbits of the simplest type x and y [4]. Originally [8], it was assumed that it is this subcritical Hopf bifurcation that causes the immediate transition to chaotic behavior discovered by Lorenz. Actually, the chaotic behavior starts below ρ_2 [9, 4], and no change in the global behavior can be observed at ρ_2, which was also confirmed by our numerical results (see Sec. IV). It is well known at present that the prerequisites for the transition to chaos are being prepared well below ρ_2 at a value of $\rho = \rho'$ corresponding to homoclinic bifurcation (first homoclinic explosion) [4]. At ρ' there is a homoclinic orbit associated with the saddle point at the origin (unstable manifold of the origin is contained in the stable manifold). This leads to the appearance of an unstable strange invariant set consisting of a countable infinity of periodic orbits, an uncountable infinity of aperiodic orbits, and an uncountable infinity of trajectories terminating in the origin. A subset of this strange invariant set then becomes the stable strange Lorenz attractor at some value $\rho_1 < \rho_2$. The fixed points $C^{\pm}$ are always the foci of the "eyes" of the Lorenz attractor. Below ρ_1, the strange invariant set cannot be detected by random numerical simulations as all trajectories still seem to tend to either of the two fixed points $C^{\pm}$. However, our numerical results presented in Sec. IV indicate that the appearance of the strange invariant set at ρ' is reflected in the change of the character of the trajectories corresponding to the initially empty Malkus waterwheel.

It is instructive to discuss also the idealized case of a frictionless wheel, having zero braking force, which corresponds to $\nu = 0$. This special case is not satisfactorily described by Eqs. (12) and (13) as it would correspond to the combination of $\sigma = 0$ and $\rho = \infty$. For $\nu = 0$, we can still keep the relations (10c), (11a), and (11d), and instead of the relations (10a), (10b) and (11b), (11c) introduce the following modified formulas:

$$\rho = \frac{\pi A g r^2 q_1}{K^2 I(\infty)} \tag{16}$$

and

$$a_1 = \frac{K I(\infty)}{\pi A g r^2} y , \tag{17a}$$

$$b_1 = -\frac{K I(\infty)}{\pi A g r^2} z + \frac{q_1}{K} . \tag{17b}$$

Using these modified definitions, Eqs. (7) for $n = 1$ become

$$\dot{x} = \frac{(1+\Delta)\, y/K - \Delta\, x\, e^{-\tau}}{1 + \Delta(1 - e^{-\tau})} , \tag{18a}$$

$$\dot{y} = \rho x - y - xz , \tag{18b}$$

$$\dot{z} = xy - z . \tag{18c}$$

As for the case when $\nu \neq 0$, the behavior of the wheel as $\tau \to \infty$ is given completely by the limit version of the above equations:

$$\dot{x} = y/K , \tag{19a}$$

$$\dot{y} = \rho x - y - xz , \tag{19b}$$

$$\dot{z} = xy - z . \tag{19c}$$

For this set of equations, the origin is again a fixed point for arbitrary ρ. However, in this case there are no other fixed points. The Lyapunov exponents at the origin are

$$\lambda_{1,2} = -\frac{1}{2} \pm \left(\frac{1}{4} + \frac{\rho}{K}\right)^{1/2}, \quad \lambda_3 = -1 .$$

For $\rho < -\frac{K}{4}$, both λ_1 and λ_2 are complex and there are inward spirals near the origin. For all other ρ, all three exponents are real. For $-\frac{K}{4} \leq \rho < 0$, all three are negative. Thus, the origin is a totally attracting point for all $\rho < 0$, and even the frictionless wheel ultimately stops in this case under the effect of gravity, regardless of the magnitude of the initial spin imparted to it. When $\rho > 0$, we find that $\lambda_2 > 0$ and the origin is a saddle point. For a nonzero initial spin, the initial conditions for the empty wheel never seem to lie on the stable manifold of this saddle point and thus the solution of Eqs. (19) always escapes to infinity for $\rho > 0$. Our numerical calculations show that after some initial transient oscillations, for large τ the solutions of Eqs. (19) become monotonous such that $z \approx \rho$ and $xy \approx \rho$. Substituting

$$y = \frac{\rho}{x} \tag{20a}$$

into Eq. (19a) gives

$$x = \pm(2\rho\tau/K + C)^{1/2}, \tag{20b}$$

C_0 being a constant of integration. The approximate results in Eqs. (20) together with $z = \rho$ describe quite well the numerical results for very large τ. Therefore, provided $q_1 > 0$, a frictionless wheel with nonzero initial spin would always monotonously increase its speed up to infinity as $\tau \to \infty$ as a consequence of the absence of a braking term in Eq. (19a). Such a wheel would never behave in a chaotic way.

Both sets of Eqs. (13) and (19) contain the same nonlinearities in the second and third equations. Only the first, linear equations of the two sets are different. However, this seemingly small difference results in significantly different behaviors of the respective solutions. In particular, while the solutions of Eqs. (19) are never chaotic, those of Eqs. (13) can be. Thus, it is the presence of friction that is a prerequisite for the chaotic behavior of this system. Also, unlike the solutions of Eqs. (19), the solutions of Eqs. (13) are always confined to a finite region near the origin of the (x, y, z) phase space [2, 5].

III. HIGHER HARMONICS OF WATER DENSITY P

For each n, the two Eqs. (7a) and (7b) constitute an autonomous system of two linear equations for the unknown functions $a_n(t)$ and $b_n(t)$ with $\omega(t)$ being a variable coefficient determined in advance by the solution of the system of the three controlling equations (12). Using definitions (11a) and (11d), one can write Eqs. (7a) and (7b) for a particular n in the form

$$\dot{a} + a = nxb\ , \tag{21a}$$

$$\dot{b} + b = -nxa + C\ . \tag{21b}$$

Here we dropped the subscript n for convenience of notation and set $C = q_n/K$. Many properties of the solutions of Eqs. (21) can be determined without knowing the exact form of the function $x(\tau)$, which can be either constant, chaotic, almost periodic or periodic.

Property 1. For given n, the form of $a(\tau)$ and $b(\tau)$ is independent of C with the amplitude of a and b proportional to C. There is no such simple scaling with n.

Property 2. All volume (area) elements of the two-dimensional phase space (a,b) do contract uniformly. This follows from the fact that the divergence of the velocity vector in phase space is equal to a negative constant:

$$\nabla \cdot v \equiv \frac{\partial}{\partial a}(\dot{a}) + \frac{\partial}{\partial b}(\dot{b}) = -2\ . \tag{22}$$

Property 3. All solutions of Eqs. (21) remain bounded in the phase space for all times. From Eqs. (21) we have

$$\frac{1}{2}\frac{d}{d\tau}(a^2 + b^2) = \frac{C^2}{4} - a^2 - \left(b - \frac{C}{2}\right)^2\ . \tag{23}$$

The right-hand side of this equation is negative everywhere outside the circle of radius $C/2$ centered at the point $(0, C/2)$. Therefore, all points on a trajectory lying outside of this circle move towards the origin and those lying inside it move away from the origin. This circle is fully contained in the circle of radius C centered at the origin. Therefore, as $\tau \to \infty$, all trajectories starting outside of this larger circle are asymptotic to it. In particular, any trajectory starting inside this circle can never get out of it. Properties 2 and 3 are analogous to the properties of the Lorenz equations [2, 5].

Property 4. Equations (21) are equivalent to the following set of integral equations:

$$a(\tau) = e^{-\tau}\left(a(0) + n\int_0^\tau x(\tau)b(\tau)e^{\tau}d\tau\right)\ , \tag{24a}$$

$$b(\tau) = C + e^{-\tau}\left(b(0) - C - n\int_0^\tau x(\tau)a(\tau)e^{\tau}d\tau\right)\ . \tag{24b}$$

These equations offer the possibility of iterative solutions. When substituting some starting approximations $a^{(i)}$ and $b^{(i)}$ for a and b on the right-hand sides of Eqs. (24), the left-hand sides give new approximations $a^{(i+1)}$ and $b^{(i+1)}$ to start another cycle of iteration. For example, starting with $a^{(0)}(\tau) = b^{(0)}(\tau) = 0$, one gets, after an infinite number of iterations, the formal solution

$$a(\tau) = e^{-\tau}\Big(a(0)\cos[nf(\tau)] + [b(0) - C]\sin[nf(\tau)] + C\sum_{k=0}^{\infty}(-1)^k n^{2k+1} g_{2k+1}(\tau)\Big)\ , \tag{25a}$$

$$b(\tau) = e^{-\tau}\Big(-a(0)\sin[nf(\tau)] + [b(0) - C]\cos[nf(\tau)] + C\sum_{k=0}^{\infty}(-1)^k n^{2k} g_{2k}(\tau)\Big)\ . \tag{25b}$$

Here

$$f(\tau) = \int_0^\tau x(u)du\ ,$$

$$g_0(\tau) = e^{\tau}\ ,$$

$$g_{k+1}(\tau) = \int_0^\tau x(u)g_k(u)du\ .$$

The domain of convergence of the series occurring in Eqs. (25) depends on the form of $x(\tau)$. The case of $C = 0$ is special. It follows from Eqs. (25) that in this case the trajectory always ends up at the origin of the phase space, regardless of the initial conditions and of the form of $x(\tau)$. This is the only case when the origin becomes a fixed point. This simply means that a given mode in the water density (height of water in individual compartments) can be excited only if the amplitude q_n of the corresponding mode in the distribution of water inflow is nonzero.

Property 5. The form of Eqs. (25) leads us to the

following important property: Let $\bar{a}(\tau)$ and $\bar{b}(\tau)$ be a solution of Eqs. (21). Then the solution of Eqs. (21) with arbitrary initial conditions $a(0)$ and $b(0)$ is

$$a(\tau)=\bar{a}(\tau)+e^{-\tau}\{\alpha\cos[nf(\tau)]+\beta\sin[nf(\tau)]\}\ , \quad (26a)$$

$$b(\tau)=\bar{b}(\tau)+e^{-\tau}\{\beta\cos[nf(\tau)]-\alpha\sin[nf(\tau)]\}\ , \quad (26b)$$

where $\alpha=a(0)-\bar{a}(0)$ and $\beta=b(0)-\bar{b}(0)$. This can be easily verified by direct substitution into Eqs. (21). Therefore, knowing one solution, one can easily construct all remaining solutions. Moreover, from Eqs. (26) it follows that, as $\tau\rightarrow\infty$, all trajectories converge towards a single trajectory — an attractor. From property 3 it then follows that this attractor must lie inside or on the circle of radius C centered at the origin. According to property 1 the shape of this attractor is independent of the magnitude of C. Therefore, for a given value of $x(\tau)$ (as determined by parameters ρ and σ in Sec. III), it is sufficient to investigate (numerically) this attractor for a single value of C and then scale appropriately for other values of C. The character of this attractor is determined by the character of $x(\tau)$, i.e., by the (attractor) solution of the limit (Lorenz) equations (13).

Property 6. For arbitrary T there is a solution $\tilde{a}(\tau)$ and $\tilde{b}(\tau)$ of Eqs. (21) such that $\tilde{a}(0)=\tilde{a}(T)$ and $\tilde{b}(0)=\tilde{b}(T)$. [For example, these two conditions lead always to a nonsingular system of equations for two unknowns α and β in Eqs. (26)]. Because of property 3, such a trajectory must lie from its beginning $(\tilde{a}(0),\tilde{b}(0))$ inside the circle of radius C centered at the origin. As $T\rightarrow\infty$ this trajectory must approach infinitesimally close to the attractor discussed above. Now, let $x(\tau)$ be a periodic function with period T, i.e., $x(\tau+T)=x(\tau)$ for all τ. Because it then follows from Eqs. (21) that $\dot{\tilde{a}}(0)=\dot{\tilde{a}}(T)$ and $\dot{\tilde{b}}(0)=\dot{\tilde{b}}(T)$, the trajectory $(\tilde{a}(\tau),\tilde{b}(\tau))$ must also be periodic with period equal to T (or a fraction of T). Using this periodic orbit as $(\bar{a}(\tau),\bar{b}(\tau))$ in Eqs. (26), we can see that it attracts all other trajectories and consequently it constitutes the limit cycle of Eqs. (21). In this case, there cannot exist any chaotic attractor. A special case of a periodic function is a constant. If $x(\tau)=x_c=\text{const}$, then

$$\tilde{a}(\tau)=C\frac{nx_c}{1+n^2x_c^2}\ , \quad \tilde{b}(\tau)=C\frac{1}{1+n^2x_c^2}$$

is a fixed point attracting, according to Eqs. (26) again, all the trajectories. Thus we have shown, that the character of the limit behavior of higher modes a_n and b_n is fully determined by that of the controlling equations (12). If $x(\tau)$ [angular velocity $\omega(t)$] goes to a fixed point (uniform motion), so do a_n and b_n. If $x(\tau)$ is periodic for large times, so are a_n and b_n. The only possibility for a_n and b_n to behave chaotically is when $x(\tau)$ behaves chaotically (ends up in a chaotic attractor). In the next section we will discuss some numerical results indicating that a_n and b_n indeed always behave chaotically in this case, and show the form of their chaotic attractors. These attractors, which are contained in the circle of radius C at the origin [or in a cylinder in the (a_n,b_n,x) space], are in a sense the projections of the Lorenz-type attractors into the new subspaces of the full phase space.

IV. NUMERICAL RESULTS FOR CHAOTIC DYNAMICS

We have carried out extensive numerical calculations to study the dynamics of the rotating waterwheel and thus explore in a detailed way the Lorenz parameter space. This is done with the use of a somewhat modified program of Ref. [12] for the simultaneous solution of Eqs. (12) and (21) for an arbitrary value of n. All the calculations reported below were carried out for an initially empty wheel whose initial spin x_0 is nonzero, i.e., for $x(0)=x_0$, $y(0)=0$, $z(0)=\rho$, and $a_n(0)=b_n(0)=0$ for $n\geq 2$. In this section, we report and discuss our results.

A. Attractors for the higher harmonics

In all (a_n,b_n) subspaces, any trajectory with the above initial conditions is contained from the beginning inside the circle of radius $C_n=q_n/K$ centered at the origin (see property 3 of Sec. III). Since the motion of the wheel in the limit $\tau\rightarrow\infty$ is determined by the Lorenz model, we have found, as expected, the following four types of limit behavior: rest, uniform rotation, chaotic reversals of the spin of the wheel and periodic time dependence of spin (periodic reversals). As discussed in Sec. II, the wheel comes to rest for $\rho<1$ when the trajectory in phase space is attracted to the fixed point at the origin. Examples of the other three types of limit behavior are presented in Figs. 2–4, consecutively showing chaotic behavior, uniform rotation, and periodic reversals.

The x-z panel of Fig. 2 displays a typical Lorenz

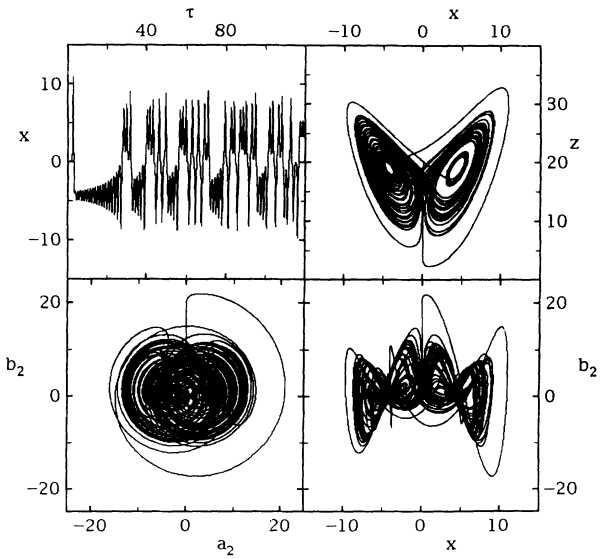

FIG. 2. Chaotic behavior: Phase-space trajectory of the Malkus waterwheel for $\sigma=4$, $\rho=20$, $\Delta=20$, $C_2=25$, $x_0=0.01$. Plot of the spin variable x as a function of the dimensionless time τ and projections on several coordinate planes of the phase space are shown.

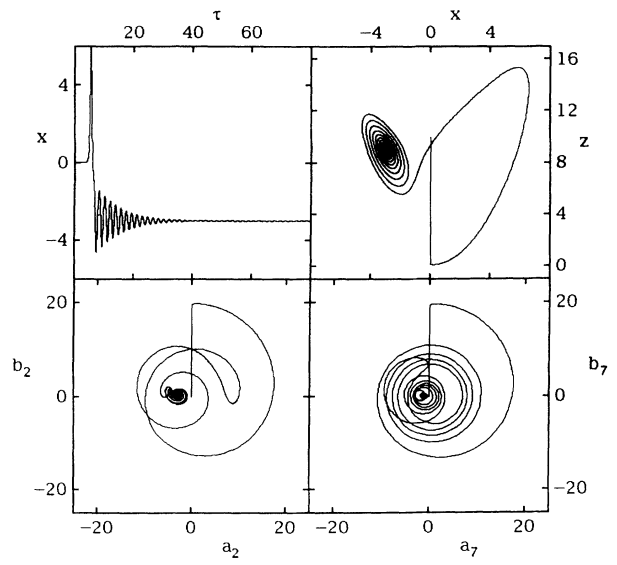

FIG. 3. Uniform limit rotation: Phase-space trajectory of the Malkus waterwheel for $\sigma=3.75$, $\rho=10$, $\Delta=20$, $C_2=C_7=20$, $x_0=10^{-4}$. The wheel eventually rotates counterclockwise with constant angular velocity.

strange attractor. The trajectory in the (a_n, b_n) space is also chaotic. The natures of the chaotic attractors for various n are usually not much different from each other. As n increases, the trajectory has the tendency to fold over itself even more and thus be contained in an area

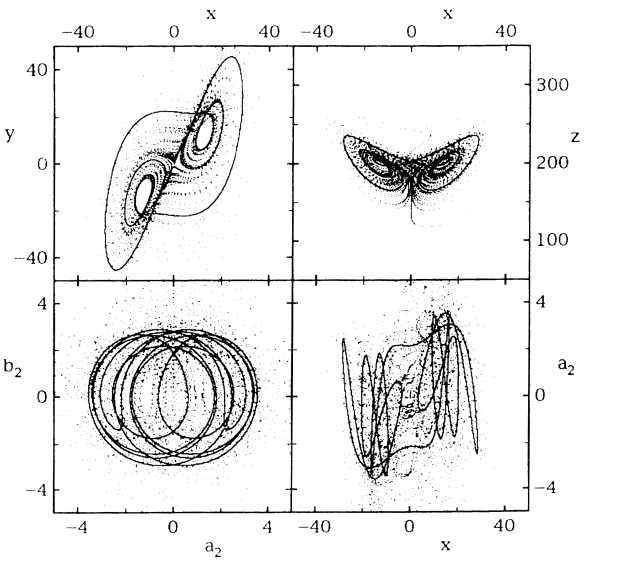

FIG. 4. Periodic limit behavior: Projections of the phase-space trajectory of the Malkus waterwheel for $\sigma=10$, $\rho=200$, $\Delta=20$, $C_2=20$, $x_0=0.01$. Only isolated points of the trajectory were plotted every 0.01 units of τ. This enabled us to visualize the periodic limit orbit (x^3y^3), which after a large number of traversals shows up as a closed continuous line on the background of a cloud of isolated dots that correspond to the initial transient phase.

that shrinks close to the origin. However, this process is not monotonically decreasing with n. In the (a_n, b_n, x) subspace, the chaotic attractor is helical. The limit uniform rotation in Fig. 3 corresponds to the fixed point C^- and is opposite to the direction of the initial spin. Comparing the trajectories in the (a_2, b_2) and (a_7, b_7) subspaces in Fig. 3 reveals how much more the trajectory folds over on itself the larger the value of n. Figure 4 shows a case when the trajectory is attracted to a stable periodic orbit of the type x^3y^3 in the notation of Sparrow [4]. In this notation an x represents one spiral around C^+ and a y one spiral around C^-.

B. Bifurcation diagrams

It is known [4,5] that the simple Lorenz model yields a rich assortment of various behaviors. Systematics of various bifurcations and periodic windows have been studied in detail [4,6] only for $\sigma = 10$, $\beta = 8/3$, and $\rho > 0$. Sparrow also presents some estimates of the expected behavior for $\sigma = 10$, arbitrary β, and $\rho > 0$. However, we are not aware of any detailed study of the distribution of the various types of the limit behavior in the (σ, ρ, β) parameter space. Thus we have undertaken to obtain such a map of at least a part of the (σ, ρ) parameter space directly for the Malkus waterwheel equations (12) with the empty-wheel initial conditions and for an arbitrarily selected initial spin $x_0 = 0.01$ and $\Delta = 20.0$. To a large extent, our results will also apply to the general Lorenz model with $\beta = 1$. We have investigated the Poincaré return map of Eqs. (12) with the Poincaré section chosen to be the plane $z = \rho - 1$. This is the plane containing the two fixed points $C^{\pm}$ which most trajectories for $\rho > 1$ loop around. For every trajectory investigated, we have calculated the first 500 downward crossings through the Poincaré section. Because we are interested here in the $\tau \to \infty$ behavior, we have skipped the first 200 crossings in the hope that the initial transient phase will end, well before the first 200 loops are completed. After this, we have recorded the y coordinate of the next 300 crossing points. If the trajectory has been attracted to the fixed point C^+ or C^- in the meantime, we plot a single dot at the y coordinate of the respective fixed point. If the trajectory has been attracted to a periodic orbit, one gets one or more discrete y values according to the complexity of the given periodic orbit. If the trajectory is chaotic, one gets a continuous band of y values. For a series of fixed values of σ, this procedure has been repeated for a large number of equidistant values of ρ, giving us a good picture of the series of bifurcations taking place as ρ changes.

Some examples of the bifurcation diagrams obtained in this way are presented in Figs. 5–10. For $\rho < 1$, the trajectory (starting at $z = \rho$) crosses the $z = \rho - 1$ plane only once as it moves towards the fixed point at the origin. Thus no points are recorded in this region in the bifurcation diagrams obtained. Immediately above $\rho = 1$, only one dot at $y = (\rho - 1)^{1/2}$ or $y = -(\rho - 1)^{1/2}$ can be found for each ρ, which corresponds to one of the two fixed points $C^{\pm}$. Above the fixed-point region, there starts chaotic

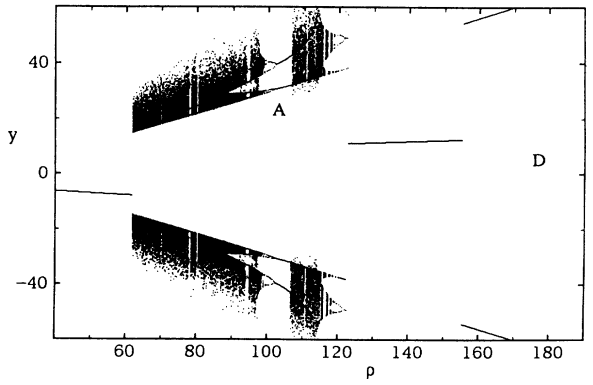

FIG. 5. Bifurcation diagram of the Poincaré return map of the Malkus waterwheel equations (12). These equations were integrated for 750 equidistant values of ρ in the interval shown. The coordinates of the first 500 downward crossings through the plane $z=\rho-1$ were calculated. Of these, the first 200 (transient phase) were skipped, for the next 300 a dot was plotted at the y coordinate of the crossing point. $\sigma=1.76$, $\Delta=20$, $x_0=0.01$. The regions of topologically identical limit periodic orbits in various bifurcation diagrams are labeled by identical letters.

behavior corresponding to areas continuously filled with dots. (For the smallest values of σ, a trajectory can end up at one of the two fixed points $C^{\pm}$, also for some values of ρ above the chaotic region, such as in Fig. 5 when the trajectory ends in a fixed point for $\rho < 61.6$, and then again for $122.3 < \rho < 154.9$.) The chaotic region contains many periodic-orbit windows of varying width. At one or both edges of some of these periodic-orbit windows, one can clearly observe cascades of period-doubling bifurcations. We have labeled the widest windows by the letters A, B, and C. The same letters in different bifurcation diagrams correspond to topologically identical periodic orbits near the center of these windows. The letter D denotes the region of periodic orbits that most probably extends up to $\rho=\infty$. In Sparrow's notation, the periodic orbits in the A and B windows are of type x^2y^2 while those in the C and D windows are of type xy.

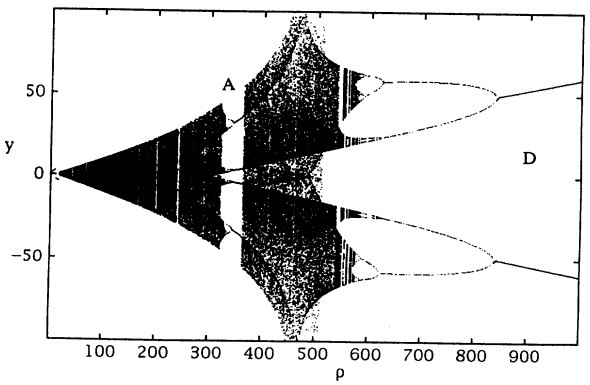

FIG. 6. Bifurcation diagram for $\sigma=10.0$. All other parameters are the same as in Fig. 5.

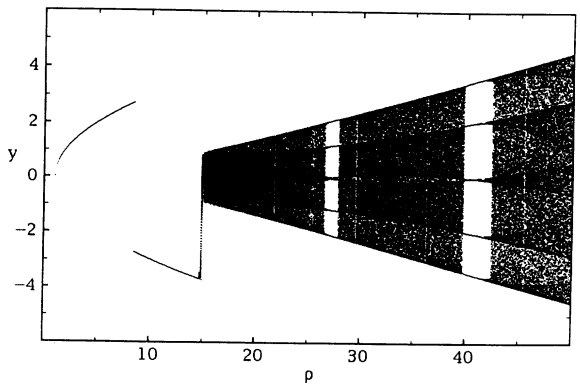

FIG. 7. The beginning of the bifurcation diagram of Fig. 6 recalculated at higher resolution.

In Figs. 5–10, only those windows are recorded that contain at least one of the equidistant values of ρ at which the Poincaré return map was calculated. As the resolution was increased, new narrower windows were revealed, as can be seen when comparing Figs. 6 and 7 or 9 and 10. Note that chaos (some of which is definitely stable) and limit periodic cycles occur also for $\sigma<2$ where the fixed points are stable for all values of ρ. At the beginning of the chaotic region for $\sigma=10$ in Fig. 7, one finds the signature of metastable chaos [10] occurring for $\rho<14.97$, where some of the trajectories needed more than 200 or 500 loops to end up in one of the two fixed points $C^{\pm}$. The trajectory at $\rho=14.97$ remains chaotic at least up to $\tau=50\,000$, which corresponds to about 30 000 loops around C^+ or C^-. This value of ρ is well below the Hopf bifurcation at $\rho_2=17.5$. $\rho_2=\frac{\sigma(\sigma+4)}{\sigma-2}$ has a minimum of 14.928 203 at $\sigma=2(1+\sqrt{3})=5.464\,101\,6$. For this value of σ and for $x_0=0.01$, stable chaotic behavior starts at $\rho=14.250\,493$. In the region below ρ_2, the final path of the trajectory is highly sensitive to the initial conditions. For example, for $\sigma=2(1+\sqrt{3})$, the trajectory for $\rho=14.250\,493$ goes to a fixed point for $|x_0|<0.01$ and is chaotic for $|x_0|\geq 0.01$. For $|x_0|=1$ chaos starts at $\rho\approx 13.84$, while for $|x_0|=100$ it starts at $\rho\approx 13.0$ (see

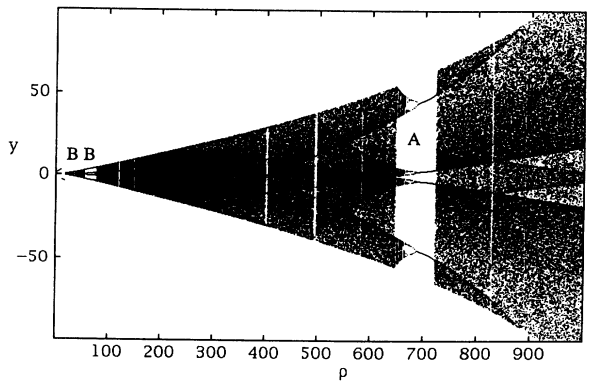

FIG. 8. Bifurcation diagram for $\sigma=15.0$. All other parameters are the same as in Fig. 5.

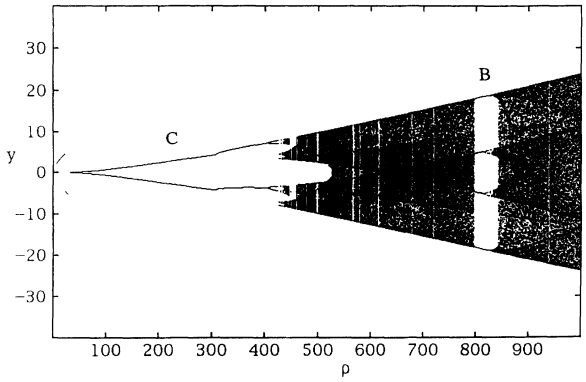

FIG. 9. Bifurcation diagram for $\sigma = 40.0$. All other parameters are the same as in Fig. 5.

also Sec. IV E and the Appendix). In Fig. 9 ($\sigma = 40.0$) what seems to be a single line starting at $\rho \approx 31.7$ immediately above the fixed-point region is actually a chaotic region with an intricate structure, as revealed at higher resolution in Fig. 10. For this value of σ, the chaotic region seems to continue above $\rho = 1000$ for another several thousand units of ρ, occasionally interrupted by periodic windows.

C. Map of the (σ, ρ) parameter space

When all the information obtained from the bifurcation diagrams is put together, one gets a crude map of part of the (σ, ρ) parameter space, as presented in Fig. 11. The dashed line denotes the value of ρ_2 at which the Hopf bifurcation occurs [7]. The shaded area bounded by heavy solid lines is the area in which chaotic limit behavior occurs. The shape of the chaotic region resembles an asymmetric arrow, with a wide stem extending obliquely upward for at least another several thousand units of ρ (a question remains: is it continuing up to infinity, and if so, in what direction?), and two thin arms situated *below* ρ_2, of which the low-ρ arm seems to extend to infinity. Figure 11 confirms previous results [4, 9] that the Hopf bifurcation takes place only after the first

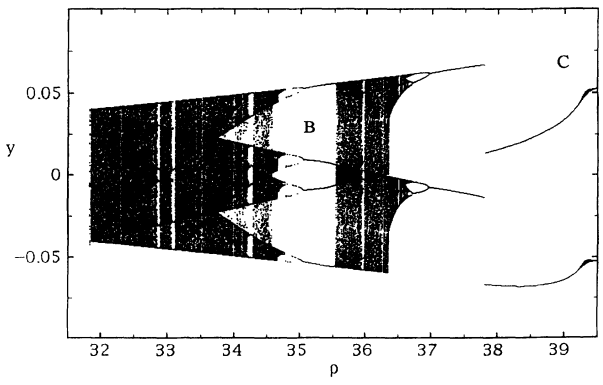

FIG. 10. Part of the bifurcation diagram of Fig. 9 recalculated at higher resolution.

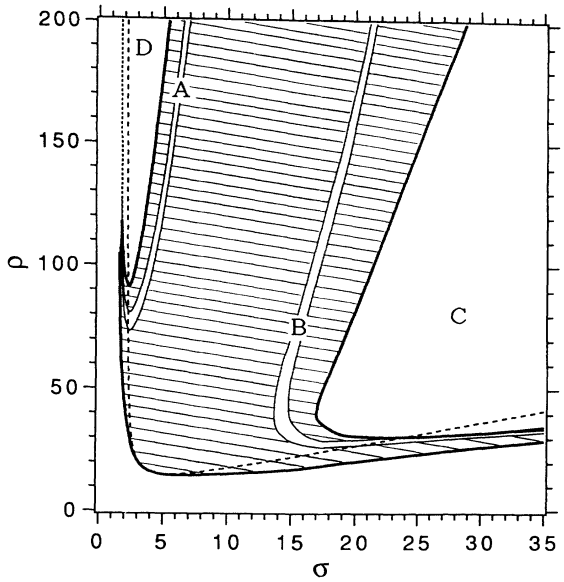

FIG. 11. Map of the vicinity of the origin of the (σ, ρ) parameter space for the Malkus waterwheel with $\Delta = 20$, $x(0) = 0.01$, $y(0) = 0$, and $z(0) = \rho$. Chaos occurs only in the shaded region bounded by solid lines. Below this region, the phase-space trajectory ends up at a fixed point. The letters A, B, C, and D denote the widest periodic windows. A and B contain periodic orbits x^2y^2 while C and D contain xy orbits. The dotted line in the upper left-hand corner separates the region of the limit-fixed points from the region of the limit periodic orbits D. The dashed line shows the position of the Hopf bifurcation at ρ_2. Only the two widest periodic windows A and B in the chaotic region are shown.

transition to chaos has occurred. The lower boundary of the chaotic region lies close to ρ_2 only in the vicinity of the minimum of ρ_2 at $\sigma = 2(1+\sqrt{3})$. We will call this region near the tip of the arrowhead, the canonical region: Lorenz canonical parameters lie in a similar region for $\beta = \frac{8}{3}$; at least between $\beta = 1$ and $\frac{8}{3}$ the map of the (σ, ρ) space seems to be similar to the one obtained here for $\beta = 1$.

The bifurcation diagrams show that the chaotic region is not continuous but contains a large number of periodic windows. Figure 11 shows the position of only the two widest ones denoted by A and B that contain topologically equivalent periodic orbits x^2y^2. The letters A and B also refer to the same windows in the bifurcation diagrams. These windows run along the stem of the arrow, bend near its head, and enter into one of its thin arms. The bending explains why the same window B occurs twice for the same value of σ in Fig. 8 or in Figs. 9 and 10. All other windows seem to be positioned roughly parallel to the windows A or B, running along the stem of the arrow, turning near the head, and entering into one of its arms. For example, the two widest windows in Fig. 7 are just the intersection of another such bent window with the $\sigma = 10$ line. Periodic windows C and D also both contain topologically equivalent orbits, this time of the xy type. Only the actual shape of these orbits

is somewhat different in C and D. The same is true for the x^2y^2 orbits in the A and B windows. It thus seems that the distribution of the periodic windows is roughly "symmetric" with respect to the "axis" of the arrow region. This hypothesis remains to be checked thoroughly for the narrower windows. However, it is immediately obvious from the bifurcation diagrams in Figs. 5–10 that the edges of the period-doubling windows at which the period-doubling cascades occur are symmetric with respect to such an axis of the arrow region.

The period-doubling edges are always those closer to this axis where the windows run parallel to the axis (or stem). Inside the narrow arms, these edges get closer to the fixed-point region. Therefore, in the windows of the A type, the cascade of the period-doubling bifurcations always occurs at the bottom edge of a window. This is the same situation as the one observed for $\beta = 8/3$, $\sigma = 10$ [4]. On the other hand, in the windows of the B type, the period-doubling cascade occurs at the bottom edge of a window, only in the low-ρ arm portion of this window. In its stem portion, the cascade occurs at the upper edge of the window, and where the window bends, both at the lower and upper edges, always assuming that one is moving along a line on which σ is constant. Therefore, the natural directions along which the sequence of various behaviors probably is always the same seem to be all the directions perpendicular to the bent periodic windows in the (σ, ρ) plane, not the lines $\sigma = \text{const}$. Figure 11 shows that it is not sufficient to investigate the behavior (series of bifurcations) of the Lorenz model for one value of σ, and assume that the results will roughly apply to all other values of σ, too.

The C window seems to have the same boomerang-like form as the B window, though it is much wider. To the right of it, there is another region with chaotic limit behavior interspersed with further periodic windows of various widths. One of these windows contains the simplest periodic orbits x and y that loop around only one of the two fixed points $C^{\pm}$ (e.g., at $\sigma = 100$, $\rho = 150$; or $\sigma = 100$, $\rho = 700$). Unstable orbits of this type are involved in the Hopf bifurcation. To our knowledge, stable orbits of this type have not been observed before in the Lorenz model.

D. Noisy periodicity

The canonical region may be best described as that part of the chaotic region that contains no periodic windows. For example, we have not detected any periodic windows in the area $4 < \sigma < 7$ and $\rho < 50$ at the resolution of $\Delta\rho = 0.0625$. The windows do bend before reaching this region. This explains the form of the Lorenz attractor of Fig. 2 extending over quite a large region of the (x, y, z) space. For most other values of the parameters σ and ρ, one can observe noisy periodicity or semiperiodicity [4], when the form of the chaotic attractor is influenced by infinitely many unstable periodic orbits left over from the period-doubling cascades in the nearby periodic windows (see Fig. 12).

The chaotic trajectory of Fig. 12 is confined in a narrow two-dimensional band in the vicinity of an unstable periodic orbit. In the (a_n, b_n, x) subspace the chaotic trajectory is also confined to a 2D band that appears to be wound around the surface of a cylinder. The attractor of Fig. 12 is an example of the asymmetric chaotic attractor. For this case, there is another attractor obtained by a mirror-image transformation $x \to -x$, $y \to -y$, to which the trajectory with the opposite x_0 would be attracted. Figure 12 explains why the corresponding part of the bifurcation diagram in Fig. 9 looks like a single line. Namely, all the downward segments of the trajectory are concentrated very close to the $x = y = 0$ axis. In this region of the (σ, ρ) plane where the braking force is large and the water inflow small, this is true for both chaotic and periodic limit behavior. The downward part of the trajectory thus corresponds to the wheel practically at rest.

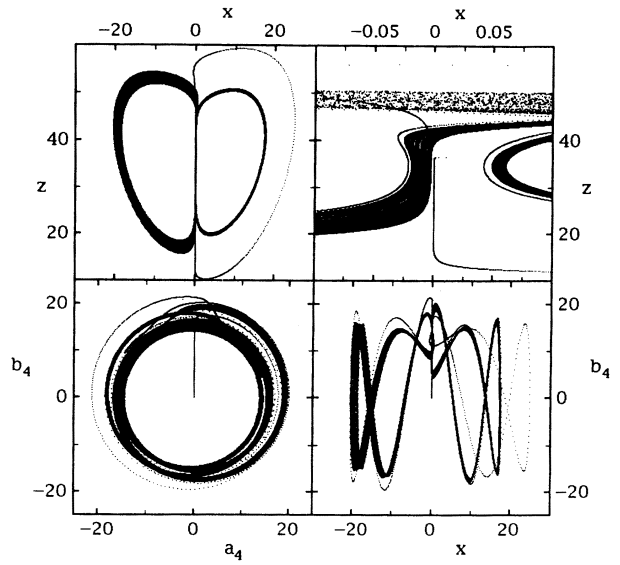

FIG. 12. Noisy periodicity attractor for $\sigma = 40$, $\rho = 36.5$, $\Delta = 20$, $C_4 = 25$, $x_0 = 0.01$. This corresponds to a point in the low-ρ arm of the arrowhead chaotic region of Fig. 11; cf. also Fig. 10. Only isolated points of the trajectory were plotted every 0.001 units of τ. This enables one to distinguish the initial transient phase showing up as dotted lines, where the separation of adjacent dots is inversely proportional to the phase-space velocity, from the limit chaotic attractor contained in a narrow 2D band in the (x, y, z) subspace. The two upper panels show the full x-z plot and a large magnification of its central part. The attractors in the (a_n, b_n, x) subspaces have the form of Möbius-like helices.

Stable chaotic behavior occurs also in the other thin arm of the arrowhead chaotic region. Here, the final destiny of the trajectory is especially sensitive to the initial conditions. As $|x_0|$ is decreased, the low-σ arm of the chaotic area extends higher along the left-hand side of the dotted line separating in Fig. 11 the limit-fixed points on the left from the D-periodic orbits on the right. For example, we have observed a stable chaotic (at least up to $\tau = 26\,000$) trajectory of the noisy-periodicity type for

$\sigma = 1.7$, $\rho = 80$, $\Delta = 20$, $C_2 = 25$, and $x_0 = 0.002$. There are also stable periodic orbits in this area of the (σ, ρ) plane.

E. First homoclinic explosion

In the end, we show that the class of the Lorenz trajectories due to an initially empty Malkus waterwheel with very small initial spin with $\rho < \rho_1$ allows us to determine easily the value ρ' at which the first homoclinic explosion occurs. For the behavior displayed in Fig. 3, our calculations show that at least for some values of σ and Δ there exists $\rho_t < \rho_1$ such that for $\rho_t < \rho < \rho_1$ a trajectory with $y(0) = 0$ and $z(0) = \rho$ ends up at the left fixed point C^- if $0 < x_0 < x_{c1}$, while for $x_0 > x_{cR}$, it ends up at the right fixed point C^+. Here $x_{cR} > x_{c1} > 0$. A trajectory starting with $-x_0$ will end up at the opposite fixed point than that starting with x_0 because if $\{x(\tau), y(\tau), z(\tau)\}$ is a solution of Eqs. (12), so is $\{-x(\tau), -y(\tau), z(\tau)\}$. In the transition interval (x_{c1}, x_{cR}) there is an infinite number of different types of trajectories ending either in C^+ or in C^-. The exact sequence of these trajectories seems to depend on ρ, and is discussed in some detail in the Appendix. For $1 < \rho < \rho_t$ all trajectories with arbitrary $x_0 > 0$ end up in the right fixed point C^+. At $\rho = \rho_t$, $x_{cR} = x_{c1} = 0$. As ρ increases above ρ_t, x_{cR}, x_{c1}, and $x_{cR} - x_{c1}$ increase, too.

In the notation introduced in the Appendix, for $\rho < \rho_t$ the trajectories are of the type $\bar{R}$ for all $x_0 > 0$. For $\rho > \rho_t$ they are of this type for $x_0 > x_{cR}$ only, while for $0 < x_0 < x_{c1}$ they are of the type $R\bar{L}$. From the nature of the first homoclinic bifurcation [4] it is obvious that $\rho_t \equiv \rho'$, the value at which the first homoclinic explosion occurs. For a very small constant value $x_0 > 0$ we thus have an almost direct transition from the $\bar{R}$ trajectories below ρ' to the $R\bar{L}$ trajectories above ρ', which can be used to determine the value of ρ'.

V. CONCLUDING REMARKS

In this paper, we have shown that the limit behavior of the Malkus waterwheel is fully controlled by the Lorenz equations with $\beta = 1$. The higher modes of the water density are just "slaves" of the controlling Lorenz equations in the sense that these modes have strange attractors only when the Lorenz equations have such attractors. We have generated the map (see Fig. 11) of the limit behavior in the (σ, ρ) parameter plane. In this plane the chaotic region has the form of an arrow with periodic windows situated "symmetrically" with respect to the axis of the arrow. In general, both ρ and σ values are important for the determination of the limit behavior. Stable x and y periodic orbits have been observed. First homoclinic explosion can be detected easily from the change in character of the trajectories of the Malkus wheel with small initial spins.

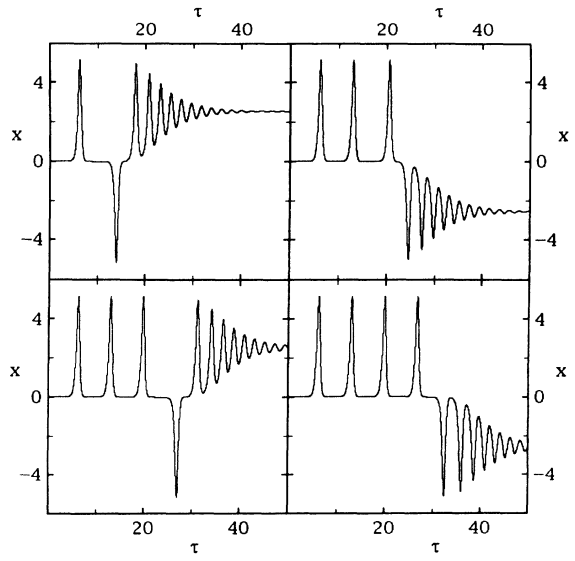

FIG. 13. Sensitivity to initial conditions below the chaotic region: different types of settling into a fixed point for $\sigma = 3.75$, $\rho = 7.5$, $\Delta = 20$. Starting from upper left, clockwise: $RL\bar{R}$ ($x_0 = 0.000\,677\,2$), $RRR\bar{L}$ ($x_0 = 0.000\,677\,415\,8$), $RRRL\bar{R}$ ($x_0 = 0.000\,677\,415\,854\,65$), $RRRR\bar{L}$ ($x_0 = 0.000\,677\,415\,854\,676\,5$).

ACKNOWLEDGMENTS

We would like to thank Professor S. H. Strogatz for bringing this problem to our attention (see Ref. [3]), and M. K. Ali for making us aware of Ref. [12] and providing us with a version of it. M.K. is grateful to the Japanese Science and Technology Agency for financial support. This research was also partially supported by a grant to G.G. from the Natural Sciences and Engineering Research Council of Canada.

TABLE I. Initial spin required for various types of trajectories for $\sigma = 3.75$, $\rho = 7.5$, and $\Delta = 20.0$.

Trajectory type	Lowest x_0	Highest x_0	i	Estimate of $x_{c,i} - x_{c,i-1}$
$R\bar{L}$	0_+	0.000 677 007	1	6.77×10^{-4}
$RL\bar{R}$	0.000 677 008	0.000 677 210	2	2×10^{-7}
$RR\bar{L}$	0.000 677 211	0.000 677 415 73	3	2×10^{-7}
$RRL\bar{R}$	0.000 677 415 74	0.000 677 415 79	4	6×10^{-11}
$RRR\bar{L}$	0.000 677 415 80	0.000 677 415 854 63	5	6×10^{-11}
$RRRL\bar{R}$	0.000 677 415 854 645	0.000 677 415 854 650	6	2×10^{-14}
$RRRR\bar{L}$	0.000 677 415 854 660	0.000 677 415 854 676 5	7	2×10^{-14}
$\bar{R}$	0.000 677 415 854 676 6	∞		

APPENDIX

In this Appendix we discuss the nature of the transition interval (x_{c1}, x_{cR}) of Sec. IV E for $\sigma = 3.75$. In this case $\rho_t \approx 7.4663466$. For ρ just above ρ_t, while the transition interval still remains extremely narrow, it already contains an infinite number of further division points $x_{c1} < x_{c2} < x_{c3} < \cdots < x_{cR}$, such that when $x_{c,2i-1} < x_0 < x_{c,2i}$, the trajectory ends up at the right fixed point C^+, and when $x_{c,2i} < x_0 < x_{c,2i+1}$, the trajectory ends up at the left fixed point C^-.

For all $x_0 > 0$, the trajectory in the x-z plane first makes a loop about the right fixed point C^+. We denote this part of the trajectory as R. Let us denote all later loops of (almost) the same radius about the right fixed point C^+ again as R and those about the left fixed point C^- as L. We refer to the final inward spiral about the right and left fixed points as $\bar{R}$ and $\bar{L}$, respectively. In our notation, $x_{c0} = 0$. A trajectory with $x_{c,2i} < x_0 < x_{c,2i+1}$, $i = 0, 1, 2, \ldots, \infty$ is of the type $R^{i+1}\bar{L}$, while that with $x_{c,2i-1} < x_0 < x_{c,2i}$, $i = 1, 2, \ldots, \infty$ is of the type $R^i L\bar{R}$, where R^n means n subsequent loops about the right fixed point. For example, the trajectory in Fig. 3 is of the type $R\bar{L}$, while trajectories of the type $RL\bar{R}$, $RRR\bar{L}$, $RRRLR\bar{R}$, and $RRRRR\bar{L}$ can be found in Fig. 13. Finally, a trajectory with $x_{cR} < x_0 < \infty$ is of the type $\bar{R}$. We conjecture that all trajectories with $x_0 = x_{ci}$, $i = 0, 1, 2, \ldots$ end up at the origin, the trajectory with $x_0 = x_{cR}$ is a periodic one, not ending in any of the three fixed points, i.e., of the type R^∞, and that the point x_{cR} is the accumulation point of the sequence $\{x_{ci}\}$. This conjecture is based on numerical data we have obtained.

For $\sigma = 3.75$, $\rho = 7.5$, and $\Delta = 20.0$ (see Fig. 13), we have found examples of the following types of trajectories: $RL\bar{R}$, $RR\bar{L}$, $RRL\bar{R}$, $RRR\bar{L}$, $RRRL\bar{R}$, $RRRR\bar{L}$, and, of course, the most common ones, $R\bar{L}$ and $\bar{R}$. Using the value of 0.005 for the time step of the fixed-step-size Runge-Kutta fourth-order differential-equation solver of Ref. [12], we have calculated more than 60 trajectories in the transition interval (x_{c1}, x_{cR}) and its immediate vicinity. The lowest and highest values of x_0 for which various types of trajectories were found and the estimates for the first few points x_{ci} based on these results are presented in Table I. For this case, $x_{cR} - x_{c1} \approx 4 \times 10^{-7}$. In this very narrow interval, the sensitivity of the form of the trajectory to the initial conditions is extremely high. The same picture was found when integrating the trajectories with smaller precision. The consequence of the decreased precision was just the shift of all the points x_{ci} to the left by the same amount. This seems to indicate that the above-described structure of the transition interval (x_{c1}, x_{cR}) is real, not just an artifact of the finite computer precision.

As ρ is increased further, x_{cR}, x_{c1}, and $x_{cR} - x_{c1}$ start to grow rapidly, and many more different types of trajectories can be found between x_{c1} and x_{cR} than at $\rho = 7.5$. For example, at $\rho = 10$, $x_{c1} \approx 25.09$, and $x_{cR} \approx 70.63$, and some examples of the trajectories we found are $RL^{10}\bar{R}$ (25.099), $RL^9R\bar{L}$ (25.1), $RL^5R^2\bar{L}$ (25.3), $RL^4R\bar{L}$ (25.5), $RL^4R^2\bar{L}$ (25.6), $RL^4\bar{R}$ (25.8), $RL^3R\bar{L}$ (26.0), $RL^3\bar{R}$ (27.0), $RL^2\bar{R}$ (30.0), $RLR^2LR\bar{L}$ (35.0), $RL\bar{R}$ (40.0), $R^2\bar{L}$ (50.0), $R^2L^2\bar{R}$ (55.0), $R^3\bar{L}$ (60.0), $R^3LR^2L\bar{R}$ (65.0), $R^6\bar{L}$ (70.0), $R^7L\bar{R}$ (70.5), $R^9L\bar{R}$ (70.6), and $R^{15}\bar{L}$ (70.62). The numbers in parentheses are the corresponding values of ρ.

* Present address: Department of Physics and Astronomy, Hunter College of the City University of New York, 695 Park Avenue, New York, NY 10021.

[1] W. V. R. Malkus, Mem. Soc. R. Sci. Liege, Collect. 6° **IV**, 125 (1972).
[2] E. N. Lorenz, J. Atmos. Sci. **20**, 130 (1963).
[3] S. H. Strogatz (unpublished).
[4] C. Sparrow, *The Lorenz Equations: Bifurcations, Chaos, and Strange Attractors*, Applied Mathematical Sciences Vol. 41 (Springer-Verlag, Berlin, 1985).
[5] E. A. Jackson, *Perspectives of Newtonian Dynamics* (Cambridge University Press, Cambridge, 1989), Vol. 2, p. 138.
[6] M.-z. Ding and B.-l. Hao, Commun. Theor. Phys. (Beijing) **9**, 375 (1988).
[7] J. E. Marsden and M. McCracken, *The Hopf Bifurcation and its Applications* (Springer-Verlag, New York, 1976), p. 142.
[8] J. B. McLaughlin and P. C. Martin, Phys. Rev. A **12**, 186 (1975).
[9] J. L. Kaplan and J. A. Yorke, Commun. Mater. Phys. **67**, 93 (1979); Ann. N.Y. Acad. Sci. **316**, 400 (1979).
[10] J. A. Yorke and E. D. Yorke, J. Stat. Phys. **21**, 263 (1979).
[11] R. Abraham and C. Shaw, *The Visual Mathematics Library: Vol. 3 — Dynamics* (Ariel, Santa Cruz, 1985).
[12] J. A. Yorke, DYNAMICS, A Program for IBM PC Clones (University of Maryland, College Park, 1988).

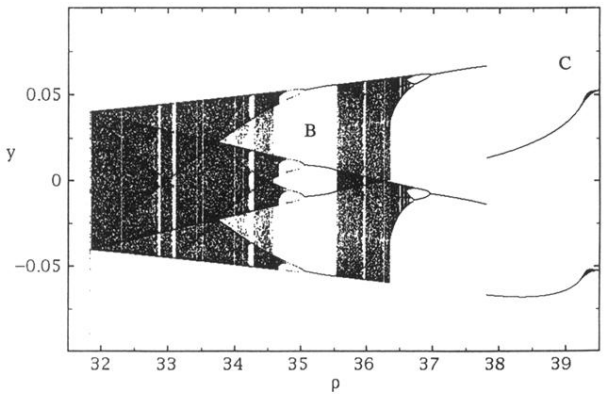

FIG. 10. Part of the bifurcation diagram of Fig. 9 recalculated at higher resolution.

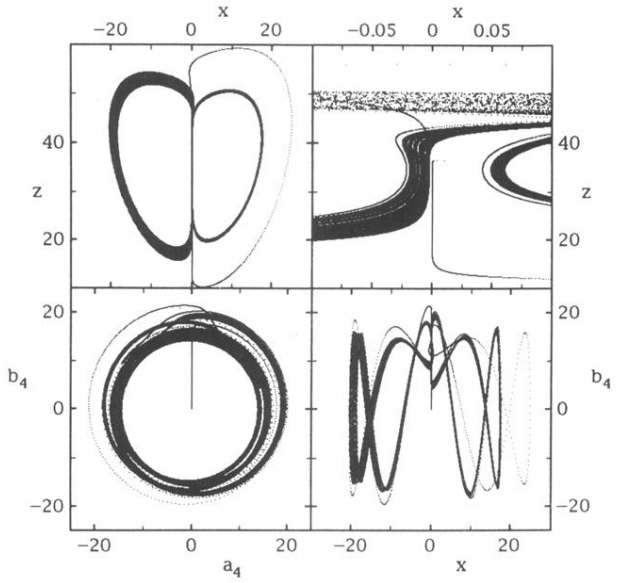

FIG. 12. Noisy periodicity attractor for $\sigma = 40$, $\rho = 36.5$, $\Delta = 20$, $C_4 = 25$, $x_0 = 0.01$. This corresponds to a point in the low-ρ arm of the arrowhead chaotic region of Fig. 11; cf. also Fig. 10. Only isolated points of the trajectory were plotted every 0.001 units of τ. This enables one to distinguish the initial transient phase showing up as dotted lines, where the separation of adjacent dots is inversely proportional to the phase-space velocity, from the limit chaotic attractor contained in a narrow 2D band in the (x, y, z) subspace. The two upper panels show the full x-z plot and a large magnification of its central part. The attractors in the (a_n, b_n, x) subspaces have the form of Möbius-like helices.

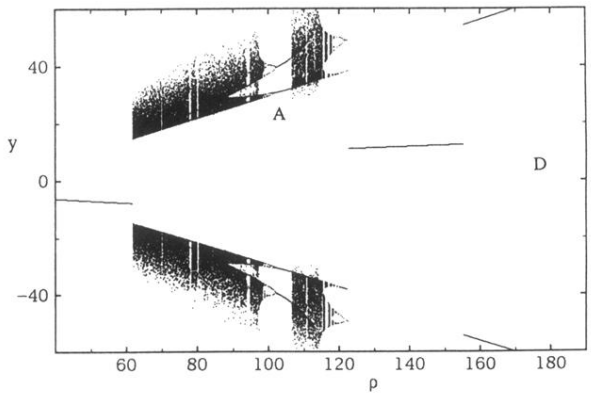

FIG. 5. Bifurcation diagram of the Poincaré return map of the Malkus waterwheel equations (12). These equations were integrated for 750 equidistant values of ρ in the interval shown. The coordinates of the first 500 downward crossings through the plane $z=\rho-1$ were calculated. Of these, the first 200 (transient phase) were skipped, for the next 300 a dot was plotted at the y coordinate of the crossing point. $\sigma = 1.76$, $\Delta = 20$, $x_0 = 0.01$. The regions of topologically identical limit periodic orbits in various bifurcation diagrams are labeled by identical letters.

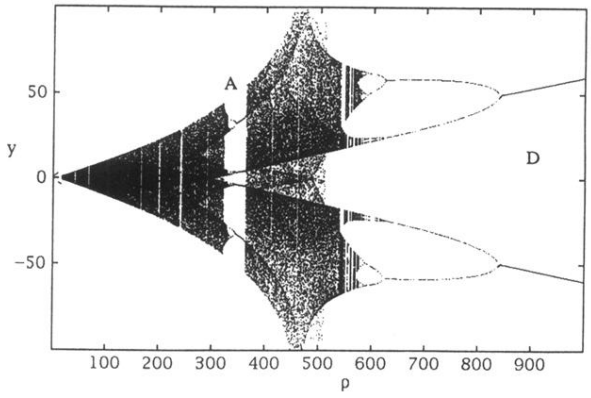

FIG. 6. Bifurcation diagram for $\sigma = 10.0$. All other parameters are the same as in Fig. 5.

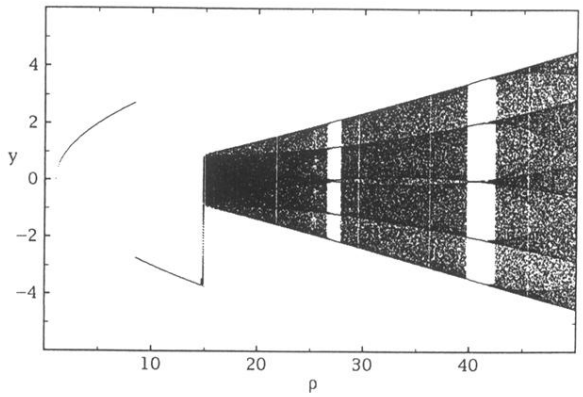

FIG. 7. The beginning of the bifurcation diagram of Fig. 6 recalculated at higher resolution.

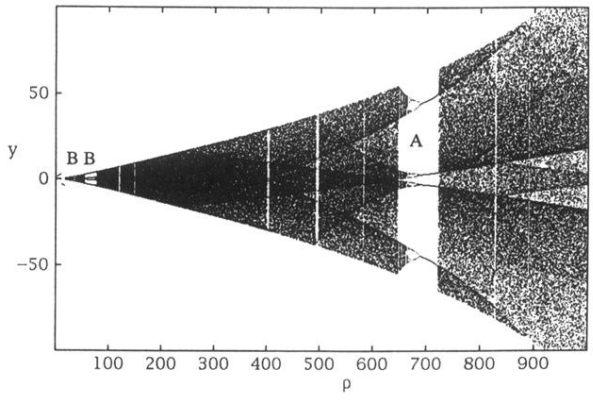

FIG. 8. Bifurcation diagram for $\sigma = 15.0$. All other parameters are the same as in Fig. 5.

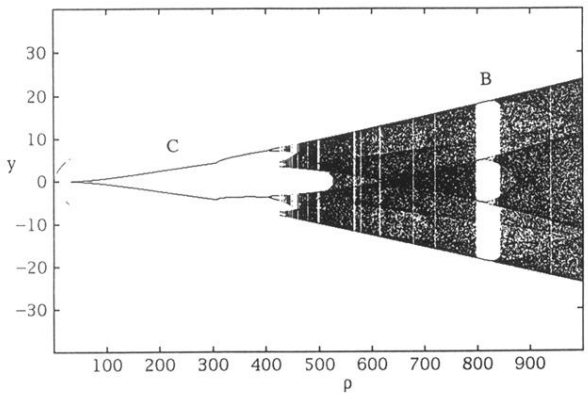

FIG. 9. Bifurcation diagram for $\sigma = 40.0$. All other parameters are the same as in Fig. 5.